JOURNAL OF COMPUTATIONAL PHYSICS **92**, 456–481 (1991)

Multi-domain Simulations of the Time Dependent Navier–Stokes Equations: Benchmark Error Analysis of Some Nesting Procedures

TERRY L. CLARK AND WILLIAM D. HALL

National Center for Atmospheric Research,
*Boulder, Colorado 80307**

Received March 31, 1989; revised September 29, 1989

This paper presents a benchmark error analysis of various approaches for treating multiple domain calculations within an anelastic finite difference model. One-way and two-way interactive nesting errors with and without temporal refinement are evaluated. The two-way interactive nesting approach is one where solutions between fine and coarse grid domains are matched through the simple post insertion of data. On the other hand, the equations can be matched by using the pressure defect correction approach. It is shown that, for the present model, the two-way interactive nesting method gives identical results to multi-domain solutions using the pressure defect correction approach. The present results indicate that in this type of analastic framework, *a priori* matching of the equations is equivalent to the *a posteriori* matching of the solutions. This result is attributed to the inflexible nature of the Neumann boundary conditions on the fine mesh pressure which need to be specified from the coarse mesh. Since a large number of meterological models employ the hydrostatic assumption, it is of interest to know of nesting errors attributable to this approximation. The results presented indicate essentially equivalent error levels for both the hydrostatic and nonhydrostatic systems of equations for the present case of airflow over an isolated mountain. It is shown how nesting technology can be used in a virtual sense to reduce the central memory requirements for large array sized numerical simulations. Nesting can be used in this sense to decompose the maximum memory working space required without affecting the results. © 1991 Academic Press, Inc.

1. INTRODUCTION

This paper presents benchmark error analyses associated with multi-domain numerical fluid dynamics simulations. The analyses are relevant to modeling applications over a wide range of low Mach number flows, despite there being an emphasis on atmospheric dynamics because this is the main application of the present model. Errors associated with one-way nesting, two-way, or interactive nesting, temporal refinement, and hydrostatic versus non-hydrostatic nesting are analyzed. Errors are determined within either the framework of two-dimensional bubble collapse experiments (a free convection problem) or stratified flow past a

---

* The National Center for Atmospheric Research is sponsored by the National Science Foundation.

0021-9991/91 $3.00

three-dimensional mountain (a forced flow problem). These experiments are designed because they are associated with a sufficient level of predictability thereby allowing direct error assessment through an intercomparison of multi-domain simulations using high resolution single-domain benchmark simulations in a manner similar to [1]. The results presented could be used to assess the relative performance of other models.

A second-order finite difference non-hydrostatic anelastic model was developed by [2, 3] which was extended by [1] to include interactive grid nesting with up to three domains but without temporal refinement. The anelastic approximation assumes that the density of the fluid is horizontally uniform except in the buoyancy term of the vertical equation of motion where its full temporal and spatial variation is considered. This approximation eliminates acoustic waves that require very small time steps for explicit numerical integration [7]. A terrain following coordinate system was used by [2] in the numerically conservative manner of [4]. This model has been used for a wide range of low Mach number meteorological and fluid dynamical problems where grid sizes can range from fractions of a meter to tens of kilometers. More recently, the model has been extended to consider an arbitrary number of domains as well as temporal refinement aspects that will be discussed in this paper. A rather pleasant and well-known result of introducing temporal refinement is that it not only results in computational efficiency but also in improved accuracy arising due to the increased consistently between the scales common to the interacting domains.

A pressure defect correction, PDC, approach similar to [5] was temporarily added to the model as an alternative method of allowing the domains to interact. Instead of applying the PDC to the solution of an elliptic equation as in [5], herein it is applied to the time dependent Navier–Stokes equations. In this application of PDC we cannot improve the accuracy of the fine mesh Neumann boundary conditions once they have been initially interpolated from the coarse mesh data. In the PDC approach, solutions to the momentum equations of the interacting domains are obtained such that it is redundant to consider *a posteriori* insertion of fine mesh fluid velocity data into the coarse mesh as performed in the two-way interactive grid nesting approach. Matching of the momentum equations is achieved by adding a PDC term to the coarse mesh equations which is equal to the difference between the appropriately averaged fine mesh and the unmodified coarse mesh equations. To obtain this difference requires a first guess pressure solution for the interacting domains. The PDC approach is more costly but arguably more elegant and has been suggested by some researchers to be more accurate. It is of interest, therefore, to evaluate differences between multi-domain solutions using the PDC approach (*a priori* matching of equations) as opposed to using the simpler and less expensive interactive grid nesting procedure (*a posteriori* matching of solutions).

An option that allows the model to be run hydrostatically is used in the present paper to explore differences in the accuracy of nesting the hydrostatic and non-hydrostatic system of equations. A parametric case that is well into the hydrostatic regime is chosen because it should be physically well represented by either system of equations. This paper does not attempt to determine the physical accuracy of the two systems of equations but instead to determine if there are any significant differences in multi-domain numerical errors attributable to the basic physical assumptions. Thus, hydrostatic nested simulations will be compared only with hydrostatic benchmark simulations and similarly for non-hydrostatic cases. Both systems of equations respond non-locally to local forcing that might intuitively seem to be a basic requirement to allow properly matched equations between domains. This non-local response is due to the infinite speed of sound resulting in a three-dimensional elliptic pressure equation in the non-hydrostatic anelastic system and the two-dimensional horizontal elliptic equation used to determine the surface pressure in the hydrostatic anelastic system. The pressure solution from these two equations converge in the limit of large horizontal to vertical scale aspect ratios. It is of interest to determine whether or not these differences at intermediate aspect ratios significantly affect the accuracy of the two-way interactive nesting.

The present paper is primarily concerned with nesting errors associated with the resolved scales. The experiments are designed with enough explicit diffusion so that parasitic waves associated with the smallest scales of the fine mesh domain do not appear to represent a significant problem. The phase and group velocity errors illustrated by [25] remain a research problem within the present model framework. In most practical problems parasitic scales are often dissipated by the application of high frequency filters or the use of artificial viscosity.

It will be shown how one can take advantage of the nesting technology to limit central memory requirements. This can be achieved by a procedure that we define as *virtual nesting*, where the pressure equations for a number of equal resolution domains are solved as if there was only a single domain. In the manner described, one obtains identical results to those using a single large domain by subdividing the domain into a number of virtually nested domains. The memory saving is achieved by virtue of the local nature of the dimension reduction approach used to solve for the pressure [2, 6]. With a modest increase in data flow and accompanying computing cost overhead one can achieve a finite-difference model which is much more limited by central processing time than by the central memory availability of the computer.

The paper is organized as follows. In Section 2 the analytical equations of the model will be briefly described first in Cartesian coordinates and then in the non-orthogonal terrain following coordinates. Next the numerical form of the equations will be presented in terms of both the non-hydrostatic and hydrostatic options. The nesting procedures and particularly the PDC approach are described as it relates to the present model. In Section 3 the results of the moist and dry bubble collapse experiments are presented and in Section 4 we present the results for the forced flow over topography. Section 5 describes the virtual nesting option and we conclude the paper in Section 6.

2. Model Description

2.1. *Analytical Equations*

Using standard tensor notation the analytical form of the momentum equations is

$$\frac{\partial \bar{\rho} u_i}{\partial t}+\frac{\partial(\bar{\rho} u_j u_i)}{\partial x_j}=-\frac{\partial p''}{\partial x_i}+\delta_{i3}\left(\bar{\rho} g B-g\frac{p''}{C^2}\right)+\frac{\partial \tau_{ij}}{\partial x_j}, \tag{1}$$

where u_i $(i=1,2,3)$ represents the velocity components in the x, y, and z orthogonal Cartesian coordinates, respectively. The density of the fluid is represented by $\bar{\rho}(z)$, the perturbation pressure by p'', the buoyancy by B, and subgrid scale mixing by the stress tensor, τ_{ij}. (τ, without subscripts, will also be used to denote the time increment index.) The constants g and C are the gravitational acceleration and the adiabatic speed of sound. In the anelastic framework acoustic waves are eliminated, [7], by putting the local time derivative of the fluid density to zero resulting in the mass conservation equation

$$\frac{\partial \bar{\rho} u_i}{\partial x_i}=0. \tag{2}$$

The buoyancy, B, in (1) couples the dynamics and the thermodynamics. In this model, B consists of terms representing the buoyancy due to potential temperature. the buoyant effects of the water vapour in the air and the drag due to cloud water, rainwater, and cloud ice. B will be described in more detail in Section 2.2. The various thermodynamic field variables of the model are treated with the conservation equation

$$\frac{\partial \bar{\rho}\phi}{\partial t}+\frac{\partial(\bar{\rho} u_j \phi)}{\partial x_j}=S_\phi+\frac{\partial}{\partial x_j}\left(\bar{\rho} K_h \frac{\partial \phi}{\partial x_j}\right), \tag{3}$$

where the arbitrary scalar field variable ϕ may represent the total potential temperature, θ, the water vapour mixing ratio of the air, q_v, or one of the condensed water substance mixing ratios such as cloud water, q_c, rainwater [8], or cloud ice [9]. S_ϕ represents the various source/sink terms due to latent heat release or conversion terms between various cloud variables. K_h is the eddy mixing coefficient for the thermodynamic variables which treats subgrid scale mixing in the simple first-order sense. The subgrid scale mixing for the momentum is also treated using a first-order closure

$$\tau_{ij}=\bar{\rho} K_m D_{ij}, \tag{4}$$

where D_{ij} is the deformation tensor and K_m is the eddy mixing coefficient for the momentum. K_m is determined using the closure theory of [10, 11].

The model is transformed from the orthogonal Cartesian system of equations to a non-orthogonal terrain following system. This transformation allows the model to be applied to problems involving flow over topography. The vertical coordinate is transformed from z to η, where

$$\eta = (z-h)/\sqrt{G} \tag{5}$$

and

$$\sqrt{G} = 1 - h/H \tag{6}$$

is the Jacobian of the transformation. H is the height of the outermost model domain and $h = h(x, y)$ is the height of the topography. $\eta = 0$ represents the material surface in the transformed equations at which the nonlinear lower velocity boundary condition reduces to $\omega = 0$, where ω is the velocity component normal to $\eta =$ constant surfaces. One can derive the transformed equations using any consistent mathematical procedure such as the chain rule or vector tensor analysis. The chain rule is applied here in the usual manner where horizontal derivatives transform as

$$\left.\frac{\partial}{\partial x}\right|_z = \left.\frac{\partial}{\partial x}\right|_\eta + G^{13}\frac{\partial}{\partial \eta} \tag{7}$$

$$\left.\frac{\partial}{\partial y}\right|_z = \left.\frac{\partial}{\partial y}\right|_\eta + G^{23}\frac{\partial}{\partial \eta}, \tag{8}$$

where the partial derivatives

$$G^{13} = \frac{\partial \eta}{\partial x} = \frac{1}{\sqrt{G}}\left[\frac{\eta}{H} - 1\right]\frac{\partial h}{\partial x} \tag{9}$$

$$G^{23} = \frac{\partial \eta}{\partial y} = \frac{1}{\sqrt{G}}\left[\frac{\eta}{H} - 1\right]\frac{\partial h}{\partial y} \tag{10}$$

are represented using tensor notation.

Using (5) through (10) it is easy to demonstrate that a conservation equation of the form

$$\frac{\partial}{\partial t}(\bar{\rho}\phi) + \frac{\partial}{\partial x}(\bar{\rho}u\phi) + \frac{\partial}{\partial y}(\bar{\rho}v\phi) + \frac{\partial}{\partial z}(\bar{\rho}w\phi) = S_\phi \tag{11}$$

in the Cartesian system transforms to

$$\frac{\partial}{\partial t}(\bar{\rho}\sqrt{G}\phi) + \frac{\partial}{\partial x}(\bar{\rho}\sqrt{G}u\phi) + \frac{\partial}{\partial y}(\bar{\rho}\sqrt{G}v\phi) + \frac{\partial}{\partial \eta}(\bar{\rho}\sqrt{G}\omega\phi) = \sqrt{G}S_\phi \tag{12}$$

in the terrain following system, where

$$\omega = (w + \sqrt{G}G^{13}u + \sqrt{G}G^{23}v)/\sqrt{G} \tag{13}$$

is the velocity normal to $\eta = \text{constant}$ surfaces. For further details on the model the interested reader is referred to [1, 2, 3, 12].

2.2. *Numerical System of Equations*

The full three-dimensional system of equations will be shown in their numerically approximated form using Schuman type numerical operators,[1] [24]. In the following equations ρ represents $\sqrt{G}$ times the $\bar{\rho}(z)$ shown previously. The three momentum equations for the Cartesian components of velocity transform from (1) to:

$$\begin{aligned}\delta_{2t}(\bar{\rho}^{x}u) &+ \delta_x(\overline{\bar{\rho}^{x}u}^{x}\bar{u}^{x}) + \delta_y(\overline{\bar{\rho}^{y}v}^{x}\bar{u}^{y}) + \delta_\eta(\overline{\bar{\rho}^{\eta}\omega}^{x}\bar{u}^{\eta}) = -\delta_x(\sqrt{G}p) - \delta_\eta(\sqrt{G}G^{13}\bar{p}^{x\eta})\\ &+ \delta_x(\sqrt{G}\tau_{11}) + \delta_y(\overline{\sqrt{G}}^{xy}\tau_{12}) + \delta_\eta(\tau_{13} + \sqrt{G}G^{13}\bar{\tau}^{x\eta}_{11} + \overline{\overline{\sqrt{G}G^{23}}^{x}\bar{\tau}^{\eta}_{12}}^{y})\end{aligned} \tag{14}$$

$$\begin{aligned}\delta_{2t}(\bar{\rho}^{y}v) &+ \delta_x(\overline{\bar{\rho}^{x}u}^{y}\bar{v}^{x}) + \delta_y(\overline{\bar{\rho}^{y}v}^{y}\bar{v}^{y}) + \delta_\eta(\overline{\bar{\rho}^{\eta}\omega}^{y}\bar{v}^{\eta}) = -\delta_y(\sqrt{G}p) - \delta_\eta(\sqrt{G}G^{23}\bar{p}^{y\eta})\\ &+ \delta_x(\overline{\sqrt{G}}^{xy}\tau_{12}) + \delta_y(\sqrt{G}\tau_{22}) + \delta_\eta(\tau_{23} + \overline{\overline{\sqrt{G}G^{13}}^{y}\bar{\tau}^{\eta}_{12}}^{x} + \sqrt{G}G^{23}\bar{\tau}^{y\eta}_{22})\end{aligned} \tag{15}$$

$$\begin{aligned}\mu_h\{\delta_{2t}(\bar{\rho}^{\eta}w) &+ \delta_x(\overline{\bar{\rho}^{x}u}^{\eta}\bar{w}^{x}) + \delta_y(\overline{\bar{\rho}^{y}v}^{\eta}\bar{w}^{y}) + \delta_\eta(\overline{\bar{\rho}^{\eta}\omega}^{\eta}\bar{w}^{\eta})\}\\ &= -\delta_n(p) + g(\bar{\rho}^{\eta}\bar{B}^{\eta} - \frac{1}{\gamma R_d}\overline{(p/T)}^{\eta})\\ &\quad + \mu_h\left\{\delta_x(\overline{\sqrt{G}}^{x}\tau_{13}) + \delta_y(\overline{\sqrt{G}}^{y}\tau^{23}) + \delta_\eta(\tau_{33} + \overline{\overline{\sqrt{G}G^{13}}^{\eta}\bar{\tau}^{\eta}_{13}}^{x} + \overline{\overline{\sqrt{G}G^{23}}^{\eta}\bar{\tau}^{\eta}_{23}}^{y})\right\}.\end{aligned} \tag{16}$$

μ_h is a flag which is set equal to one when the system is non-hydrostatic and to zero when its is hydrostatic. $B = \theta''/\bar{\theta} + \varepsilon q''_v - q_c - q_r$ is the buoyancy. The double-primed terms in B represent the deviations of the field from the horizontally uniform environment. In this model, [1], θ is decomposed as $\theta = \bar{\theta}(z) + \theta'(z) + \theta''(\vec{x}, t)$, where $\bar{\theta}$ represents an environment having a constant stability and $\bar{\theta} + \theta'$ represent the full hydrostatically balanced environment with arbitrary stability. The τ_{ij} terms represent the numerically approximated subgrid scale mixing terms as in [2]. The mass continuity equation transforms from (2) to

$$\delta_x(\bar{\rho}^{x}u) + \delta_y(\bar{\rho}^{y}v) + \delta_\eta(\bar{\rho}^{\eta}\omega) = 0 \tag{17}$$

---

[1] Schuman type operators have been used throughout the paper to represent the numerical equations. For an arbitrary dependent variable ϕ and independent variable ξ we have

$$\phi^{\xi} = [\phi(\xi + \Delta\xi/2) + \phi(\xi - \Delta\xi/2)]/2$$

$$\delta_\xi\phi = [\phi(\xi + \Delta\xi/2) - \phi(\xi - \Delta\xi/2)]/(\Delta\xi),$$

where ξ could be any of x, y, η, or τ.

and the ω relation is approximated as

$$\bar{\rho}^{\eta}\sqrt{G}\omega = \bar{\rho}^{\eta}w + \overline{\sqrt{G}G^{13}\overline{\bar{\rho}^{x}u}^{\eta}}^{x} + \overline{\sqrt{G}G^{23}\overline{\bar{\rho}^{y}v}^{\eta}}^{y}. \tag{18}$$

The remaining conservation equations transform to the form already shown in [12] and are solved using the second-order in time and space scheme, [13–15], and will not be shown. The numerical scheme shown in (14)–(17) is second order [16, 17].

Two approaches are used in solving (14) through (18). The first approach is to assume non-hydrostatic pressure balances by putting $\mu_h = 1$ in (16). We then derive an equation for $\delta_{2t}(\bar{\rho}^{\eta}\omega)$ by appropriately combining (14)–(16) and (18). We combine this ω tendency equation with (14) and (15) and take their respective derivatives to form a prognostic divergence equation. Since (17) constrains all divergences to be zero this prognostic divergence equation reduces to a diagonostic elliptic equation for the pressure. In the most general case the numerical form of this pressure equation has a 25 point stencil. We refer the interested reader to [2] for the method used to solve for p in its nonhydrostatic form. In deriving the $\delta_{2t}(\bar{\rho}^{\eta}\omega)$ equation one obtains terms commonly referred to as the Christoffel terms which involve derivatives of h times quadratic combinations of the velocity components. By numerically approximating the Cartesian velocity component equations prior to forming the $\delta_{2t}(\bar{\rho}^{\eta}\omega)$ equation we obtain a numerically consistent form to the Christoffel terms such that momentum and kinetic energy are conserved to order Δt^2 with respect to the nonlinear advection terms. This approach is similar to that of [4] and is that used by [2]. If one attempts to apply the numerical approximations to the ω tendency equation, as in [18], then identical solutions and conservation properties can be obtained only if one were to use the equivalent numerical form for the Christoffel and remaining advection terms. This is extremely tedious and it is more convenient to transform the numerical equations to form the ω tendency equation. The transformation has in no way changed the physical variables that we wish to conserve. It is for this reason that we apply the numerical approximations at the particular stage shown.

The second approach to solving (14) though (18) is to assume hydrostatic pressure balances by putting $\mu_h = 0$ in (16). A solution for p for this model which forces mass conservation is described in Appendix A. This approach is similar to that used by [19] in a sea breeze model and subsequently by [20] in a frontal scale model. The u and v fields are stepped forward in time using (14) and (15) after solving for p and ω is then stepped forward using (17). The modifications required to convert a non-hydrostatic model to a hydrostatic one are relatively minor. One of the reasons for introducing such an option in the present model is to assess numerical and physical errors associated with the commonly used hydrostatic assumption. It is much easier to assess such differences within one model than between two different models where there are typically further discretization differences.

2.3. *Multiple Domain Procedures*

There are many problems in fluid dynamics in which higher spacial resolution is required in only a limited portion of the computational domain. Grid nesting allows one to focus on such desired regions of the domain and obtain higher spacial resolution with computational efficiency. Figure 1 shows a schematic of the grid structure of two models for a two-dimensional cross section in x and η. A staggered grid system [2] is employed where the density and other thermodynamic variables are defined in the center of the grid boxes, the velocities at the surfaces of the grid boxes and the stress terms at the corner of the grid boxes.

The inner domains are always located such that each boundary of the fine mesh domain collocates with a grid surface of the interacting coarse mesh. Grid surfaces are defined as the planes at which velocity components, directed normal to the plane, are located. For example, the two $x-y$ planes of a grid are located at w positions. Furthermore, all coarse mesh grid surfaces within a fine mesh domain must collocate with fine mesh grid surfaces, i.e., the grid ratios between interacting domains must be integers. The coarse meshes are first stepped forward in time. Conditions at the domain boundaries of the respective interacting inner domains are interpolated from the coarse mesh after which the fine mesh can be stepped forward in time. After the fine mesh domain is integrated in time up to the same point as the coarse mesh then fine mesh data is inserted into the coarse mesh. The procedure of interpolating boundary data from a coarse mesh is termed *one-way interaction* if no further feedback of information from the fine to coarse mesh is considered. If there is a feedback of fine mesh data then this procedure is termed *two-way interaction*. The interpolation formulae and averaging operators used are

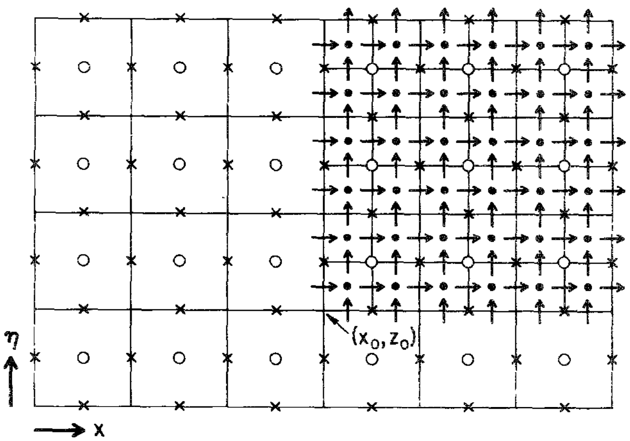

FIG. 1. Schematic of staggered grid structure for two models with a 2 : 1 nesting ratio. The circles mark coarse mesh positions of thermodynamic variables whereas the crosses mark the velocity component positions. Dots mark the fine mesh grid centered variables and the arrow marks the velocity component positions.

those described in [1]. The interpolation formulae are typically quadratic in each spatial direction. The one exception is for the interpolation of velocity component data in the logical direction of that component. In this case the formulae are cubic so that divergence constraint is maintained during interpolation. The interpolation and averaging formulae are reversible such that when the interpolation formulae are used to *spawn* a new fine mesh data set and this fine mesh data set is then averaged back onto the coarse mesh then the data on the coarse mesh remains unchanged. The starting point for all the error analyses in this paper will be the assessment of the errors of the one-way and two-way interacting schemes presented in [1]. These two schemes use the same time steps for all domains and will be termed 1-*Way CF* and 2-*Way CF*.

Another method of allowing the domains to interact is to apply a pressure defect correction (PDC], prior to updating the coarse mesh velocities. Consider two interacting domains to have the equations

$$\frac{\bar{\rho}^x u^{\tau+1}}{2\,\Delta t} + fx = pfx \tag{19}$$

for the fine mesh and

$$\frac{\bar{R}^X U^{\tau+1}}{2\,\Delta t} + FX = PFX \tag{20}$$

for the coarse mesh domain where (19) and (20) represent the x-direction horizontal momentum equations. The expressions pfx and PFX represent the pressure gradient forces whereas fx and FX represent the explicit terms such as advection, diffusion, and Coriolis. A similar procedure applies for the y- and z-direction momentum equations. The averaging operator for $\bar{\rho}^x u$ is defined as

$$\langle \bar{\rho}^x u \rangle = \frac{1}{RY \cdot RZ} \sum_j \sum_k \bar{\rho}^x u, \tag{21}$$

where $\langle \bar{\rho}^x u \rangle$ is the horizontal velocity component that the fine mesh domain would insert into the common coarse mesh region. RY and RZ are the grid ratios in the y and z (or η) directions. We define

$$\bar{R}^X U^{\tau+1} = \langle \bar{\rho}^x u \rangle^{\tau+1} \tag{22}$$

which can be achieved by adjusting FX as

$$FX^{\nu} = \langle fx \rangle + PFX^{\nu-1} - \langle pfx \rangle. \tag{23}$$

which requires that a first guess pressure solution be obtained for the coarse and fine mesh domains and ν is an interaction index.

On second and subsequent solutions for the pressure of the coarse mesh domain we substitute the pressure defect corrected value of FX^{ν} from (23) into (20). Once the pressure is calculated in this manner it is redundant to consider inserting fine mesh data into the coarse mesh. To verify that the PDC option was correctly applied, we performed redundancy tests which successfully showed (to roundoff precision) that the integration was left unaffected. This option was applied only for equal time steps and will be termed 2-*Way PDC*.

A fourth modification to the nesting procedure was to consider mixing of perturbation data for the thermodynamic variables. In [1] they mixed $\langle(\theta' + \theta'')/\bar{\theta}\rangle$. Since environmental components such as $\theta'(z)$ and $\bar{q}_v(z)$ will have slight differences between domains due to resolution effects and since the buoyancy that produces vorticity is only associated with the double primed terms, it seems reasonable to expect improved accuracy by mixing only the double primed portion of the thermodynamic variables. The choice of variable to mix between domains was taken $\langle\theta''/\bar{\theta}\rangle$ and $\langle q_v''\rangle$. In the case of moist calculations we also mix $\langle q_c\rangle$. Results of this option will be termed PM which stands for perturbation mixing.

A fifth modification to the nesting procedure was to introduce temporal refinement. This procedure involves either linearly or quadratically interpolating data from the coarse mesh to the fine. The results using this option will be termed either TF(L) for temporal refinement using linear interpolation or TF(Q) for the quadratic interpolation case.

We will now describe two sets of experiments designed to determine the relative accuracy associated with the above options.

3. Bubble Collapse Experiments

3.1. *Description of the Experiments*

A uniformly mixed region (bubble) was used by [21, 22, 1] in a linearly stratified fluid for assessing the preformance of numerical methods. In the present case, the initial environmental conditions for the two-dimensional bubble collapse experiments were defined with zero wind over a domain of 28 by 28 km in the y and z directions, respectively. The surface temperature and pressure were taken as 300°K and 1000 hPa, respectively. From $z = 0$ to 10 km, the environment was isothermal with $S = d \ln \theta/dz = g/c_p T_{\text{sfc}}$, where T_{sfc} and C_p are the surface temperature and specific heat of air at constant pressure. From $z = 10$ to 18 km, a constant environmental stability of $S = 10^{-5}\,\text{m}^{-1}$ was assumed. From $z = 18$ to 28 km the environment was again isothermal with a temperature of 243°K. Apart from q_v, this environmental structure completely defines the environmental portions of the thermodynamic variables. A region of near neutral stability was established by letting

$$\begin{aligned}\frac{\theta''}{\bar{\theta}}(\vec{x}, t = 0) = \frac{1}{4}&\left[\exp(S(z_m - z)) - 1\right]\\ &\times \left[\tanh((z - z_1)/\lambda) - \tanh((z - z_2)/\lambda)\right]\\ &\times \left[\tanh((y - y_1)/\lambda) - \tanh((y - y_2)/\lambda)\right], \qquad (24)\end{aligned}$$

where $\lambda = 300$ m, $S = 10^{-5}$ m^{-1}, $y_1 = z_1 = 12$ km, $y_2 = z_2 = 16$ km, and $z_m = (z_1 + z_2)/2$.

For the moist experiments, the relative humidity was specified at 50% throughout the experimental domain whereas for the dry experiments it was set to zero. The upper and lower surfaces at $z = 0$ and 28 km are taken as non-conducting, free-slip, rigid, and flat surfaces. The lateral boundary conditions at $y = 0$ and 28 km are taken as cyclic. A constant eddy mixing coefficient of $K_m = K_h = 60$ m^2/s for the moist experiments and 10 m^2/s for the dry experiments was assumed throughout the domain.

These initial conditions represent a diffusion chamber. As the region of neutral stability collapses the lower regions cool and upper regions heat. Figure 2 shows the

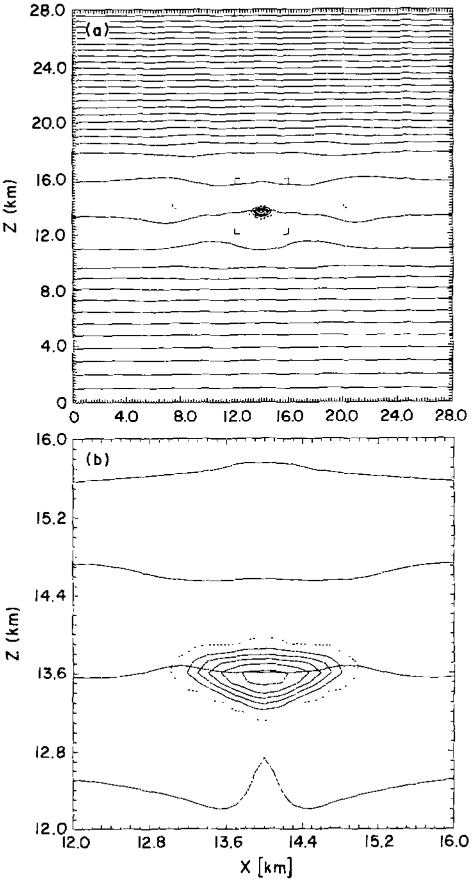

FIG. 2. θ and q_c are shown at $t = 14$ min for a moist bubble collapse experiment: (a) shows the outer domain with frame markings denoting the inner domain region. (b) shows the inner domain which is also the initial well-mixed region. Contour intervals for q_c and θ are 0.1 g kg^{-1} and 10°K in (a) and 0.1 and 5 in (b). The dashed contour represents the cloud outline where $q_c = 0.1$g kg^{-1}.

experimental framework for a moist nested simulation. Figure 2a shows the outer domain with an outline of the inner domain and Fig. 2b shows a magnification of only the inner domain region. Contours of θ and q_c are shown with the cloud centered in y and located just below the $z = 14.$ km position at $t = 14$ min. The symmetry is maintained about $y = 14$ km and there are no indictions of fine scale structures. In the case of no moisture there are only gravity waves generated which are subsequently dissipated by the diffusion coefficient. For the moist case the cooling in the lower region results in the development of a cloud. The reason for choosing such a large K_m and K_h in the moist case was to prevent the cloud from developing any boundary instabilities which quickly destroy predictability. Such instabilities prevent us from being able to discern solution differences due to either model inaccuracies from those due to the nonlinearity of the basic dynamics. Lower values of eddy mixing coefficients were tested and found unacceptable for the purposes of the present experiments.

The solutions to the govering equations are determined by integrating a single domain experiment for a period of 20 min. This benchmark model uses 280 by 280 grid points with 100 m resolution and 3 s time steps. It should be clarified that we want these benchmark solutions only to be sufficiently accurate to enable detection of significant level of errors when the resolution outside the near neutral stability region is reduced. The assumption is that by minimizing these errors (or more precisely differences) introduced through nesting, we are optimizing the nesting procedure. A second series of solutions is obtained using two nested domains. The outer domain uses 140 by 140 grid points of 200 m and exactly covers the domain of the benchmark experiment. A second domain of 4 by 4 km is centered inside the outer domain and exactly overlays the region of near neutral stability. The inner domain uses 40 by 40 grid points of 100 m resolution. The nested simulations use 3 s time steps for both domains except in the case of temporal refinement where a 6 s time step is used for the outer domain. The errors are defined as the differences between the inner domain solutions using nesting and the benchmark experiment over the identical region.

An error diagnostic employed is the relative kinetic energy error defined as

$$E_{\mathrm{ke}}(t) = \frac{\sum_j \sum_k \bar{\rho}(\Delta v^2 + \Delta w^2)}{\sum_j \sum_k \bar{\rho}(v^2 + w^2)}, \tag{25}$$

where Δv and Δw represent the differences between the benchmark solutions and the solutions obtained using nesting. Only the benchmark solutions are used in the denominator of (25). Another error diagnostic is the relative buoyancy error defined as

$$E_{\mathrm{B}}(t) = \frac{\sum_j \sum_k \bar{\rho}\, \Delta B^2}{\sum_j \sum_k \bar{\rho} B^2}, \tag{26}$$

where again ΔB represents the differences between the benchmark and nesting solutions. It should be noted that $E_{\mathrm{B}}(t)$ is biased by the fact that $B(t = 0) \neq 0$.

3.2. *Moist Results*

Figure 3 shows the $E_{ke}(t)$ and $E_B(t)$ errors versus t for six different nested calculations. The 1-*Way* results are divided by 10 and shifted for purposes of convenience of display. As noted in the earlier work of [23, 1] and others the 1-*Way* errors are considerably larger than the 2-*Way* interactive case. Towards the end of the exprtiment they are as much as 40 times larger than the most inaccurate 2-*Way* case.

The CF and PDC (pressure defect correction) simulations, using equal Δt between domains, gave nearly identical errors. The PDC results were insensitive to the number of iterations beyond the first. These findings are siginifant in that they demonstrate that it is not important whether or not one matches the momentum equations *a priori* through the pressure solutions using PDC or *a posteriori* using

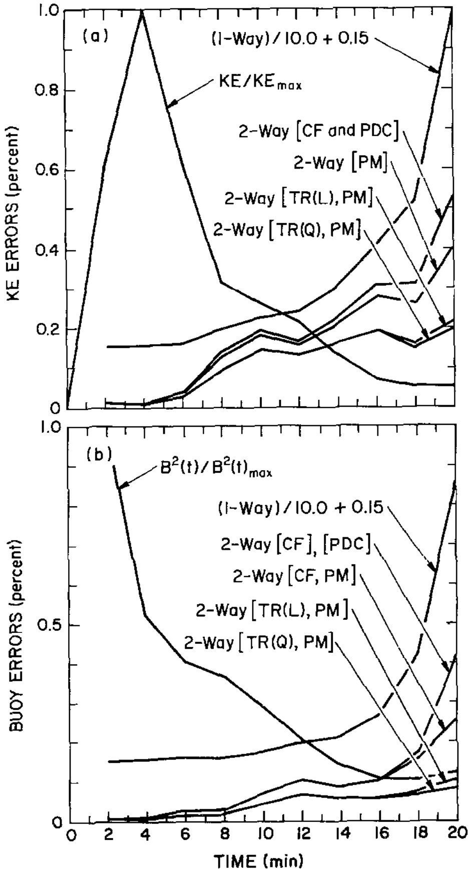

FIG. 3. Moist bubble collapse experiment error plots: (a) shows the kinetic energy errors and (b) the buoyancy errors versus time. The heavy solid line in each of these plots represents a normalized plot of the total quadratic field taken from the benchmark experiment.

post insertion of fine mesh data into the coarse mesh. The PDC is more expensive as well as more complicated. These results support the concept that typical interactive nesting used in meterology is a mathematically sound procedure.

The addition of perturbation mixing to the CF approach results in a slight reduction of errors. The addition of temporal refinement significantly reduces the errors from those using equal Δt. The reason for this improvement is probably due to the fact that in terms of Courant numbers both domains now have similar errors at the same scale of motion. This increased consistency should tend to reduce the amount of reflection at domain interfaces. Quadratic temporal refinement gives a very slight improvement in accuracy for this experiment.

Figure 4 shows w and Δw errors at $t = 10$ min. This is the time of maximum absolute errors for these experiments. Plate 4a shows the full w with a contour interval of 0.5 ms^{-1}, whereas plates 4b, c, and d show Δw errors for the 1-Way, 2-Way [CF], and 2-Way [TR(Q), PM], respectively. The scale of the errors is

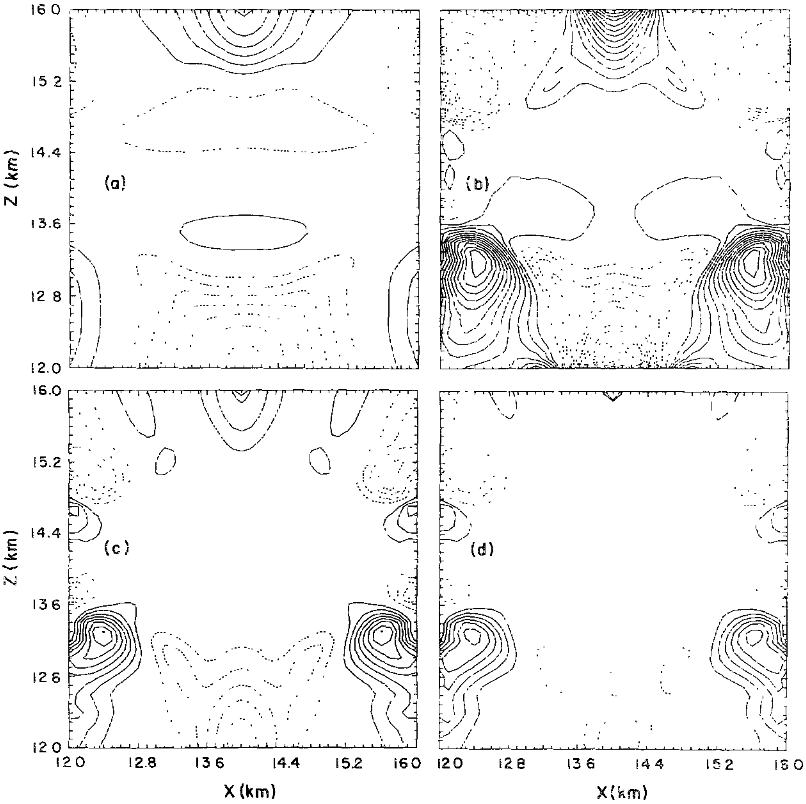

FIG. 4. w field plots for the moist bubble collapse experiments at $t = 10$ min: (a) shows the full w field with a contour interval of 0.5 m s^{-1}. (b), (c), and (d) show the Δw errors for the 1-Way, 2-Way CF, and 2-Way TR(Q) cases, respectively. The contour interval is 0.03125 m s^{-1} in these error plots.

comparible to that of the field itself. There is a noticeable difference in structure and amplitude between the 1-Way and most inaccurate 2-Way errors, whereas there is mainly a difference in amplitude between the most inaccurate and most accurate 2-Way errors.

3.3. *Dry Results*

Figure 5 shows E_{ke} and E_{B} versus t for the dry bubble collapse experiments. The character of the errors is similar to those in the moist bubble experiment. The absolute magnitude of the errors is about 6 times larger for the dry experiments than for the moist. These differences are most likely due to the smaller eddy mixing coefficient of $10\,\mathrm{m}^2\mathrm{s}^{-1}$ in the dry as opposed to the $60\,\mathrm{m}^2\mathrm{s}^{-1}$ in the moist. The CF and PDC gave exactly the same results where one extra iteration through the coarse mesh pressure solver was used in the pressure defect correction approach.

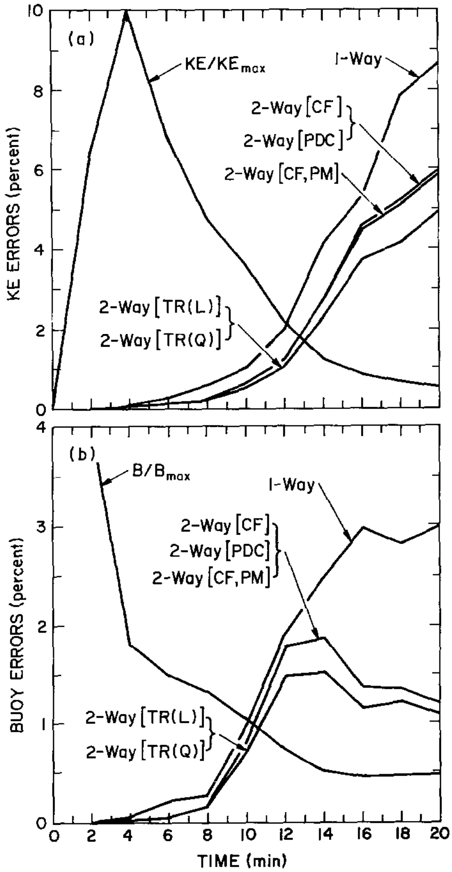

FIG. 5. Same as in Fig. 3 except for the dry bubble collapse experiment.

The temporal refinement again resulted in a systematic reduction of errors although there was an insignificant difference between linear and quadratic interpolation in time.

4. STRATIFIED FLOW PAST A THREE-DIMENSIONAL MOUNTAIN

4.1. *Description of the Experiments*

This experiment consists of a uniform flow having constant stability. $S = 10^{-5}\,\mathrm{m}^{-1}$ and mean wind speeds of $10\,\mathrm{ms}^{-1}$ and $1\,\mathrm{ms}^{-1}$ in the east–west and north–south directions flowing over an isolated mountain. The surface temperature and pressure are 300°K and 100 hPa, respectively. The mountain height, h, is taken as

$$h(x, y) = h_0/(1 + (x'/a)^2 + (y'/b)^2) \tag{27}$$

where x' and y' are distances relative to the domain center. The mountain is taken as an ellipse with $a = 25$ km and $b = 30$ km and $h_0 = 1.5$ km. The Froude number, $Fr = U/(Nh_0)$, is about $\frac{2}{3}$ for this case, where N is the Brunt–Väisälä frequency. The outermost domain is chosen as 600 by 600 km in the horizontal and 30 km in the vertical. The horizontal boundary conditions are cyclic and a Rayleigh friction and Newtonian cooling absorber is used in the top 12 km of the domain. The structure of the absorber is chosen such that $1/\tau$ is linear and varies from zero at $z = 18$ km to 1/1000 s at the domain top. As in [1] there is an applied smoothing fit at $z = 18$ km to this linear structure. Coriolis, surface drag, surface sensible heat, and moisture flux effects are all set to zero in these experiments. This experiment is designed so that the flow can be accurately treated using either the hydrostatic or non-hydrostatically approximated equations. The reason for chosing a flow that impinges on the mountain at an angle about 84° to the main axis is to produce enough asymmetry in the solution to affect nesting errors associated with matching domain stresses.

The benchmark model uses 120 by 120 by 60 grid points in the x-, y-, and z-directions. The grid sizes are taken as 5 km in the horizontal and 0.5 km in the vertical. For the two-domain model simulation the outer domain uses half the resolution of the benchmark model. The inner model is centered with respect to the outer and covers a horizontal domain of 200 by 200 km and a vertical domain of 15 km. Both the inner and outer domains have their lowest η level on the ground.

The simulations are initialized using a potential flow deviation from the initial U and V profiles such that mass continuity is satisfied. The procedure assumes that

$$\begin{aligned} \bar{\rho}^x u &= \bar{\rho}^x U - pfx(\phi) \\ \bar{\rho}^y v &= \bar{\rho}^y V - pfy(\phi) \\ \bar{\rho}^\eta \omega &= \bar{\rho}^\eta \Omega - pf\omega(\phi) \end{aligned} \tag{28}$$

where *pfx*, *pfy*, and *pfω* are the logical equivalents to the pressure gradient terms in (14), (15), and the ω prognostic equation derived by combining (14) to (16) with (18). The divergence of (28) consistent with (17) requires

$$\delta_x(pfx(\phi)) + \delta_y(pfy(\phi)) + \delta_\eta(pf\omega(\phi)) = \delta_x(\bar{\rho}^x U) + \delta_y(\bar{\rho}^y V) + \delta_\eta(\bar{\rho}^\eta \Omega). \qquad (29)$$

The existing three-dimensional non-hydrostatic pressure solver is adapted to solve (29). After ensuring a high degree of convergence, the solutions to (28) and (29) are used to initialize the simulations. The initial buoyancy is taken as zero. In order to avoid differences in results caused by solving (28) and (29) at different resolutions, the simulations start off using three domains. The first domain is taken as the coarse resolution outer domain having 10 km resolution in the horizontal. The second domain is taken as the benchmark model domain which interacts with the first domain. The third domain is the 5 km resolution inner domain which interacts with the second domain. This setup is initialized and integrated to $t = 10$ min using a 50 s time step. At $t = 10$ min all errors are identically zero. For $t > 10$ min the

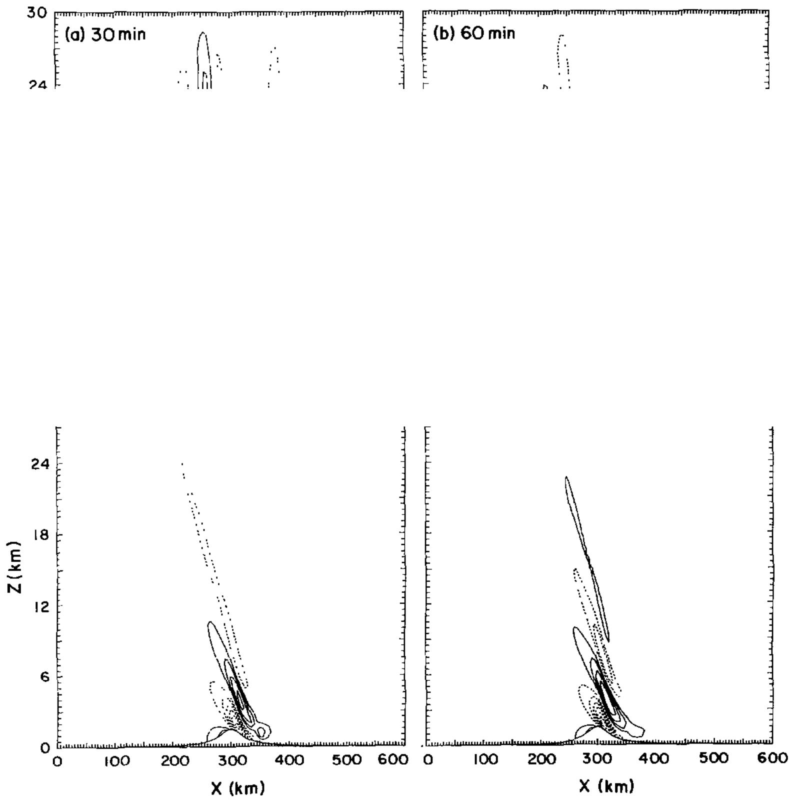

FIG. 6. Field plots of w from the non-hydrostatic benchmark model at $t = 30$, 60, 90, and 120 min., $\Delta x = \Delta y = 5$ km, and $\Delta z = 0.5$ km. The contour interval is 0.1 m s^{-1}.

benchmark and two-domain experiments are treated in a totally independent manner. The error diagnostics (25) and (26) are again used in these experiments except that the full three-dimensional difference kinetic energy is used in the numerator of (25). Instead of using the full kinetic energy of the benchmark in the denominator. only three times the energy associated with w is used. This avoids strong biases due to the mean flow and makes the percentage errors more representative of the actual errors.

4.2. *Results*

Figures 6, 7, and 8 show east-west oriented cross-sections of w for the benchmarks domain 1 and domain 2 of the 2-Way [CF] non-hydrostatic case at four times, respectively. These plots are oriented at an angle of about 6° off parallel from the mean flow and show a developing forced wave response. At $t = 30$ and 60 min there is still evidence of reflected modes above $z = 12$ km due the potential flow type of initialization. The initial buoyancy was taken as zero which results in an initial zero first time derivative on all vorticity components and in a relatively

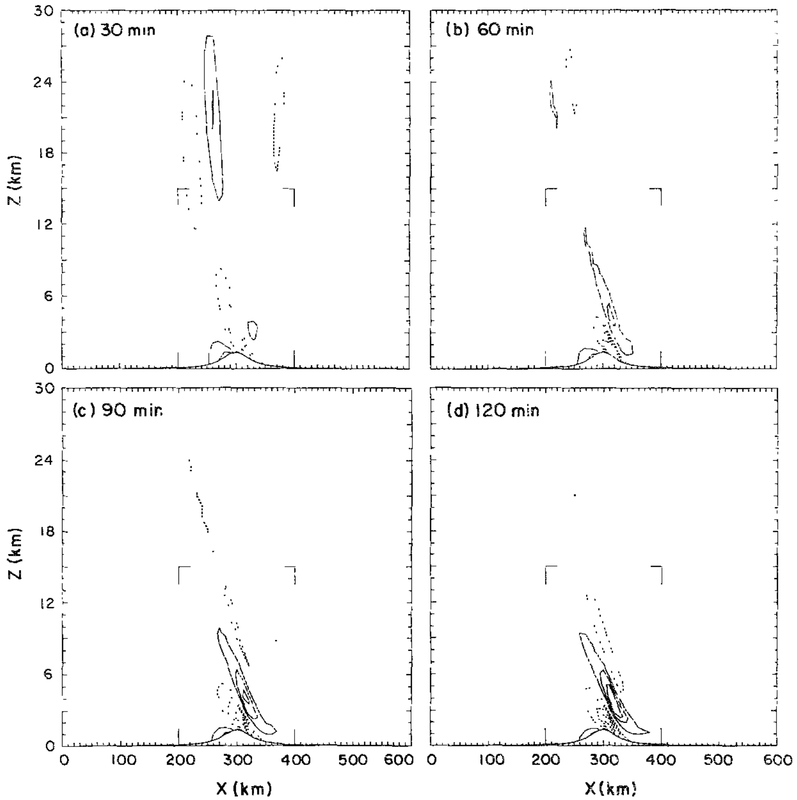

FIG. 7. Same as Fig. 6 except for a nested calculation where the outer domain used the 2-Way CF approach. Spatial resolutions are $\Delta x = \Delta y = 10$ km and $\Delta z = 1$ km. Frame markers denote position of the inner domain.

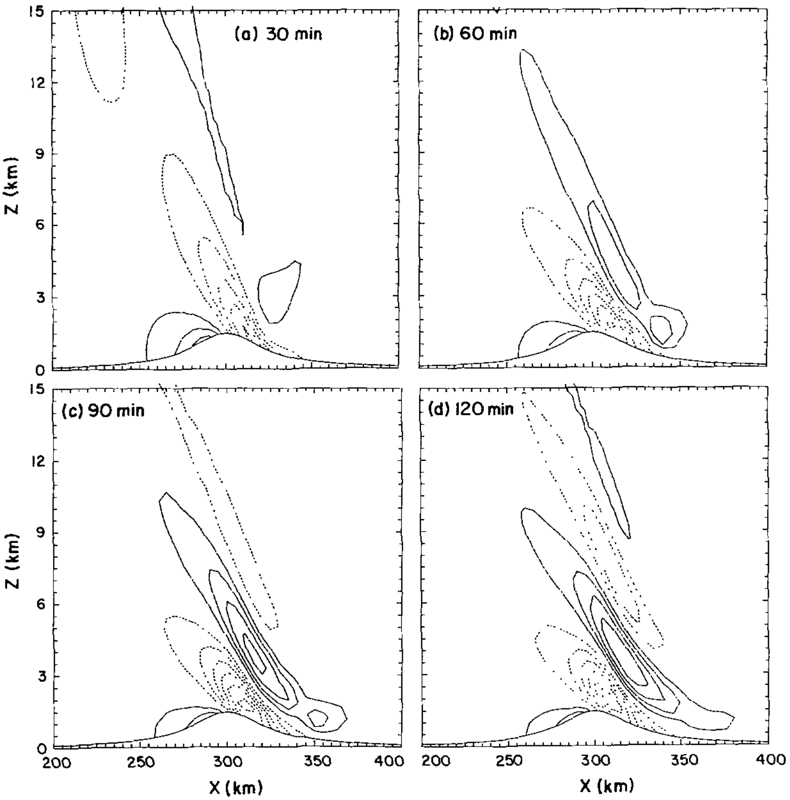

FIG. 8. Same as in Fig. 7 except inner domain is shown. Resolution here is identical to the benchmark model.

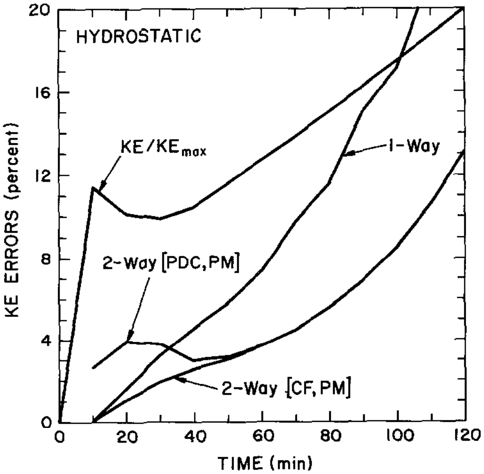

FIG. 9. $E_{ke}(t)$ error plots for the hydrostatic case stratified flow case. Note the convergence of the two 2-Way error plots in spite of their differences in initialization as discussed in text.

smooth transition from the potential flow regime to the forced wave regime. Figure 7 shows that these early reflected modes extend into the inner domain and as a result will be a part of the nesting error. Their highly temporal nature supplies a good test to the nesting technology. Figure 8 shows the inner domain solution of the [CF, PM] case and compares quite accurately with the benchmark case in Fig. 6.

The hydrostatic and non-hydrostatic solutions are almost indistinguishable from one another for this particular experiment. The solutions for the hydrostatic system of equations appears to converge rather quickly in spite of some significant differences in initial conditions. This was accidentally demonstrated by our having initialized a hydrostatic nesting case with the non-hydrostatic initial conditions at $t = 10$ min. As shown in Fig. 9, the hydrostatic [CF, PM] and [PDC, PM] cases

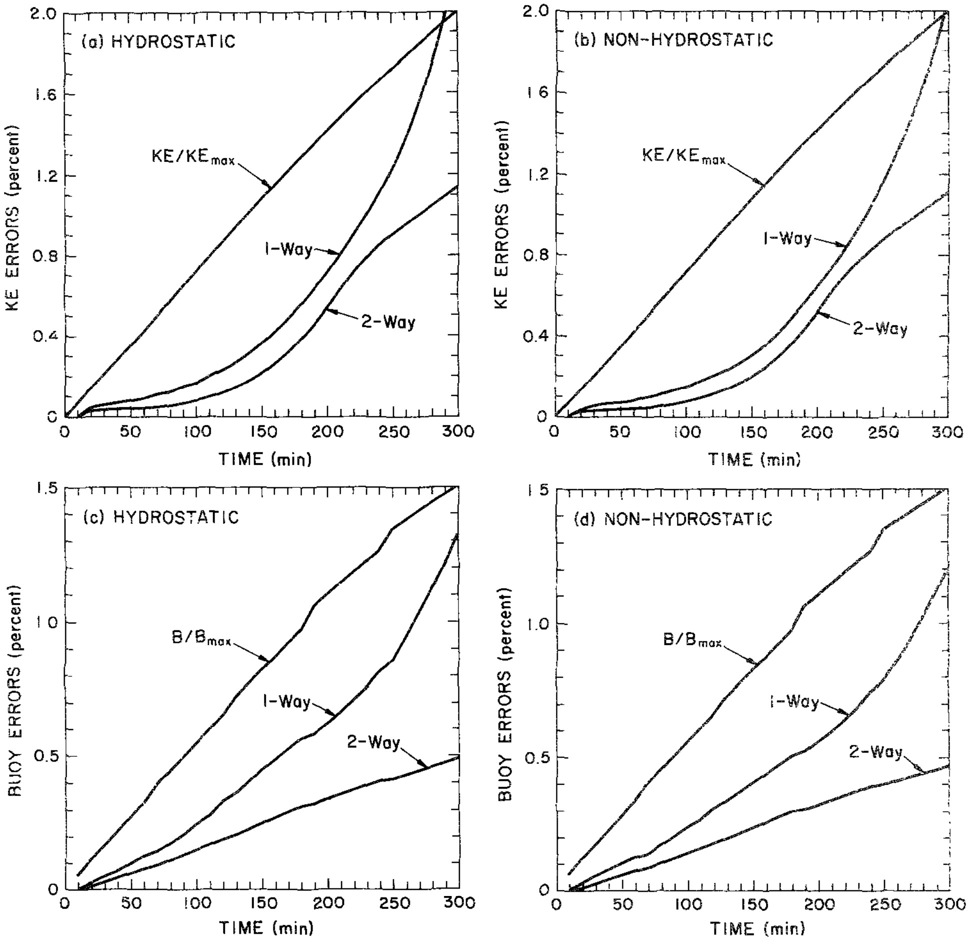

FIG. 10. Stratified flow experiment error plots: (a) and (b) show the $E_{ke}(t)$ errors for the hydrostatic and non-hydrostatic cases, respectively. (c) and (d) show the $E_B(t)$ errors for the same cases.

converged to near identical errors after about 70 min in spite of the fact that the [PDC, PM] case was inappropriately initialized. The surprising aspect of this result is that convergence occurs long before any steady state is achieved.

Fig. 10 shows the $E_{\mathrm{ke}}(t)$ and $E_{\mathrm{B}}(t)$ errors for the non-hydrostatic and hydrostatic cases. The overall relative performance of nesting is quite similar between the two systems of anelastic equations. The errors of the hydrostatic case begin to increase at a slightly greater rate than those of the non-hydrostatic case towards the end of these experiments, probably due to the increased sensitivity of the hydrostatic system to "noise" generation as compared with the non-hydrostatic system. However, for these experiments these differences are still quite small at $t = 300$ min.

As in the bubble collapse experiments, the pressure defect correction and basic 2-Way CF interaction approach give the same results for both the hydrostatic and non-hydrostatic models. This means that the post insertion of fine-mesh data into the coarse mesh is equivalent to *a priori* matching of the momentum equations through the pressure solution. In the case of these type of topography flows, the basic [CF, PM] 2-Way interaction approach is considerably less expensive than the [PDC, PM] approach.

5. VIRTUAL NESTING

The available central memory of a computer can present a serious limitation to the size of numerical experiments which can be performed. Furthermore, memory use can represent a significant fraction of computer charges for large simulations. Finite difference codes such as the present tend to be memory bound rather than CPU bound. Virtual nesting is a procedure that does not affect the accuracy of the calculation and can significantly reduce the central memory requirements needed to perform a numerical experiment requiring a large number of grid points.

In the current paper we take a single domain and divide it into four equal domains, each of which has half the number of grid points in both horizontal directions as the original domain. Since the current code requires one full field in memory for purposes of solving the elliptic pressure equation, this approach could conceivably quarter the memory requirements. However, overhead of the resident code plus other working arrays represent a considerable portion of a model's memory requirements so we realize only a fraction of this factor of four. The main consideration in virtual nesting is to ensure that these newly created inner boundaries, formed by dividing the large single domain into four nested domains, in no way affects the results. This virtual nesting approach differs from domain decomposition approaches. In the current approach, subdomains are not treated independently at each stage of the solution process and no additional iterative procedures are required. The elliptic pressure equation represents the most obvious problem in this respect. The procedure for dealing with this will now be outlined.

The present model uses a block iterative scheme to solve for the pressure. In the case of no topography, the approach reduces to a direct solver. The first step in solving for the pressure is to dimension reduce both sides of the elliptic equation in the vertical direction. This reduces the problem to solving a set of decoupled two-dimensional Helmholtz equations where the number of these equations equals the number of levels of the model. The important point is that this vertical dimension reduction can be performed for each of the virtually nested domains prior to considering solving any of the two-dimensional Helmholtz equations. The two-dimensional Helmholtz equations are then combined from each subdomain and solved as though there was logically only a single domain. This procedure, plus the storing of some extra boundary condition arrays to appropriately treat the transparent boundaries, results in a nesting procedure whose main effect is to reduce the central memory requirements of the computer. The remaining calculations performed by the model include momentum, advection, and condensation terms. These are all local operators that have been made transparent at each virtual boundary by storing the appropriate surfaces of data.

The performance of virtual nesting for the present model is shown in Fig. 11, where maximum central memory requirement is plotted against the virtual domain size. Curves 1 and 2 represent the regular code without virtual nesting using 2 : 1 and 3 : 1 word packing precision on a Cray X-MP/48. Curves 3 and 4 represent the virtually nested case, where a single array has been subdivided into four nested arrays. Again the results for 2 : 1 and 3 : 1 word packing precision are shown. As an example we see that using 5 Megawords of memory we can fit a model using a single array size of 1.8 million grid points into the X-MP/48 without virtual

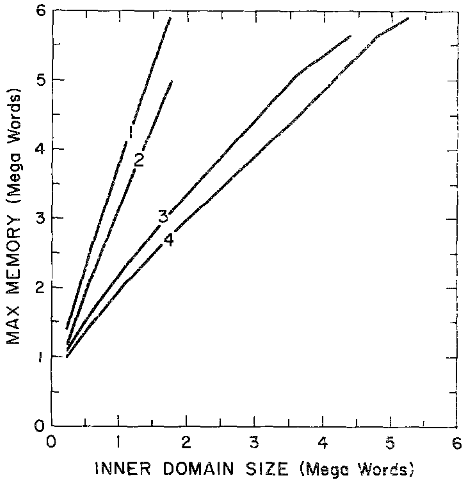

FIG. 11. Total central computer memory versus array size. The inner array size is for either a single domain (curves 1 and 2) or for the virtually nested case (curves 3 and 4). Curves 1 and 3 are for the 2 : 1 and curves 2 and 4 for the 3 : 1 word packing precision used in the central memory input/output buffers of the model. The case treated here is for no topography and with potential temperature as the only thermodynamic field variable.

nesting at a precision of 3 : 1. However, with this current virtual nesting we can fit a model using a single virtual array size of 4.2 million grid points. Or possibly more important, we can fit the 1.8 million grid point job into a reduced memory of 2.75Megawords and save considerable computer memory charges. The overhead for performing this nesting procedure is less than a 4% increase in CPU when considering array sizes larger than about one million grid points. This additional CPU charge is typically more than offset by a reduction in computer memory charges.

6. CONCLUSIONS

Two types of experimental frameworks were used to assess numerical errors associated with multiple domain or grid nesting methods. Both moist and dry bubble collapse experiments were performed in two dimensions as well as stably stratified flow over a three-dimensional isolated mountain. Multiple domain simulations were compared with single domain benchmark cases in which high resolution was employed throughout the domain.

It was found that identical results were obtained through using either the conventional 2-Way interaction nesting approch or using a pressure defect correction approach. It made no difference whether or not one matched the equations through the pressure defect correction or whether one matched the solutions by post-insertion of fine mesh data into the coarse mesh. This result is a direct consequence of the fact that the fine mesh domain must take its lateral boundary conditions from the coarse mesh and that there is no method known to the authors by which these boundary conditions can be influenced by the fine mesh domain solutions once they have been specified. The intercomparisons between the pressure defect correction and 2-Way interaction were performed only for equal time steps (no temporal refinement). The authors saw no point in taking the PDC approach any further as it is cumbersome and costly and as a result it has been dropped from the present code.

It was found that a post mixing of the purely time dependent perturbation components of the thermodynamic fields resulted in a slight improvement in accuracy. The inclusion of temporal refinement with similar Courant numbers for each domain also resulted in improved accuracy for the bubble collapse experiments. Temporal refinement has no noticeable effect on the error level for the three-dimensional mountain flow case.

Comparisons between anelastic hydrostatic and anelastic non-hydrostatic simulations of air flow over a three-dimensional isolated mountain showed almost identical nesting errors for both systems of equations. There was an indication of an increase in errors of the hydrostatic over the non-hydrostatic that was very slowly developing with time. This was attributed to the increased sensitively to "noise" in the hydrostatic system.

Virtual nesting was tested for the present code and shown to represent a practical approach of reducing central memory requirements for numerical experiments that use a large number of grid points.

APPENDIX A: HYDROSTATIC PRESSURE CALCULATION

The horizontal equations of motion can be presented as

$$\frac{\bar{\rho}^x u^{\tau+1}}{2\Delta t} + fx = -\delta_x(\sqrt{G}p) - \delta_\eta(\sqrt{G}G^{13}\bar{p}^{x\eta}) \tag{A.1}$$

$$\frac{\bar{\rho}^y v^{\tau+1}}{2\Delta t} + fy = -\delta_y(\sqrt{G}p) - \delta_\eta(\sqrt{G}G^{23}\bar{p}^{y\eta}), \tag{A.2}$$

where fx and fy represent the explicit terms of advection, diffusion, and Coriolis.

These equations are combined with the anelastic continuity equation (17) to form

$$\begin{aligned}\delta_{xx}(\sqrt{G}p) + \delta_{yy}(\sqrt{G}p) + \delta_{x\eta}(\sqrt{G}G^{13}\bar{p}^{x\eta}) + \delta_{y\eta}(\sqrt{G}G^{23}\bar{p}^{y\eta})\\ = \delta_\eta(\bar{\rho}^\eta\omega)^{\tau+1}/2\Delta t - \delta_x(fx) - \delta_y(fy).\end{aligned} \tag{A.3}$$

Summing (A.3) over vertical columns results in

$$\begin{aligned}\nabla_H^2\left\{\sum_{k=2}^{NZ-1}\sqrt{G}p\Delta\eta\right\} + \delta_x\sqrt{G}G^{13}\bar{p}^{x\eta}\big|_{\eta=\eta_b}^{\eta=\eta_t} + \delta_y\sqrt{G}G^{23}\bar{p}^{y\eta}\big|_{\eta=\eta_b}^{\eta=\eta_t}\\ = (\bar{\rho}^\eta\omega_{\eta_t} - \bar{\rho}^\eta\omega_{\eta_b})^{\tau+1}/2\Delta t - \sum_{k=2}^{NZ-1}\{\delta_x(fx) + \delta_y(fy)\}\,\Delta\eta,\end{aligned} \tag{A.4}$$

which represents the diagnostic column pressure equation which must be satisfied in order to satisfy mass continuity. The η_k positions for p are grid centered and taken as $\eta_k = (k - 3/2)\,\Delta\eta$ for $k = 1, 2, ..., NZ$. The pressure at the domain bottom, η_b is defined as $\bar{p}^\eta_{\eta_b} = (p_{k=1} + p_{k=2})/2$. Similarly, the pressure at the domain top, η_t is defined as $\bar{p}^\eta_{\eta_t} = (p_{k=NZ} + p_{k=NZ-2})/2$. The vertical recursion relation for p can be inserted into (A.4) to obtain the final elliptic equation.

The particular form for hydrostatic pressure in the model is taken as

$$\delta_\eta\, p = \frac{g\sqrt{G}}{\gamma R_d}\,\overline{(p/T)}^\eta = g\bar{\rho}^\eta\bar{B}^\eta \tag{A.5}$$

where B is buoyancy, This buoyancy is typically small in this system as it contains only deviations from an initial horizontal uniform environmental profile. This formulation results in similar magnitudes of p in (A.1) and (A.2) as in the non-hydrostatic anelastic system.

An expansion of (A.5) results in

$$p_{k+1} = \alpha_k\, p_k + \beta_k, \tag{A.6}$$

where

$$\alpha_k = \left(1 - \frac{\Delta\eta g\sqrt{G}}{2\gamma R_d T_k}\right)\bigg/\left(1 + \frac{\Delta\eta g\sqrt{G}}{2\gamma R_d T_{k+1}}\right) \tag{A.7}$$

and

$$\beta_k = g\,\Delta\eta(\bar{\rho}^{\eta}\bar{B}^{\eta})_{k+1/2}\Bigg/\left(1+\frac{g\Delta\eta\sqrt{G}}{2\gamma R_d T_{k+1}}\right). \tag{A.8}$$

Equation (A.6) leads to the identities

$$\sum_{k=2}^{NZ-1}(\sqrt{G}p\,\Delta\eta) = Ap_1 + E \tag{A.9}$$

$$\bar{p}^{\eta}_{\eta=\eta_t} = A_t p_1 + E_t \tag{A.10}$$

$$\bar{p}^{z}_{\eta=\eta_b} = A_b p_1 + E_b, \tag{A.11}$$

where

$$A = \{\alpha_1(1+\alpha_2(1+\alpha_3(1+\cdots\alpha_{NZ})))\}\sqrt{G}\,\Delta\eta \tag{A.12}$$

$$\begin{aligned} E = {} & \{\beta_{NZ-2} + \beta_{NZ-3}(1+\alpha_{NZ-2}) + \beta_{NZ-4}(1+\alpha_{NZ-3}(1+\alpha_{NZ-2})) \\ & + \cdots + \beta_1(1+\alpha_2(1+\alpha_3(1+\cdots+\alpha_{NZ-2})))\}\sqrt{G}\,\Delta\eta \end{aligned} \tag{A.13}$$

$$A_t = (1+\alpha_{NZ-1}(\alpha_1\alpha_2\alpha_3\cdots\alpha_{NZ-2})/2 \tag{A.14}$$

$$\begin{aligned} E_t = {} & \beta_{NZ-1}/2 + (1+\alpha_{NZ-1})[(\alpha_2\alpha_3\cdots\alpha_{NZ-2})\,\beta_1 \\ & + (\alpha_3\alpha_4\cdots\alpha_{NZ-2})\,\beta_2 + \cdots + \beta_{NZ-2}]/2 \end{aligned} \tag{A.15}$$

$$A_b = (\alpha_1 + 1)/2 \tag{A.16}$$

$$E_b = \beta_1/2. \tag{A.17}$$

Substituting (A.9) through (A.11) into (A.4) results in

$$\begin{aligned} & \nabla^2_H(Ap_1) + \delta_x[h_x(Z_{NZ}\overline{A_t p_1}^{x} - Z_2\overline{A_b p_1}^{x})] \\ & \quad + \delta_y[h_y(Z_{NZ}\overline{A_t p_1}^{y} - Z_2\overline{A_p p_1}^{y})] \\ & = -\nabla^2_H E - \delta_x[h_x(Z_{NZ}\overline{E_t}^{x} - Z_2\overline{E_b}^{x})] - \delta_y[h_y(Z_{NZ}\overline{E_t}^{y} - Z_2\overline{E_b}^{y})] \\ & \quad + (\bar{\rho}^{\eta}\omega_{\eta_t} - \bar{\rho}^{\eta}\omega_{\eta_b})^{\tau+1}/2\Delta t - \sum_{k=2}^{NZ-1}[\delta_x(fx) + \delta_y(fy)]\,\Delta\eta \\ & = \text{RHS}, \end{aligned} \tag{A.18}$$

where $Z_k = \eta_{k/H} - 1$.

$$D = \tfrac{1}{2}(Z_{NZ}A_t - Z_2A_b)/A \tag{A.19}$$

$$\phi = Ap_1, \tag{A.20}$$

equation (A.18) reduces to

$$\nabla^2_H\phi + 2\delta_x[h_x\overline{D\phi}^{x}] + 2\delta_y[h_y\overline{D\phi}^{y}] = \text{RHS}. \tag{A.21}$$

Once ϕ is found, p_1 is calculated using (A.20). The full pressure field is determined using (A.6). Appropriate boundary conditions for ω at the domain top and bottom are either specified (for the outer domain) or extrapolated from outer domains for a nested domain. The implementation of this hydrostatic option into the model had no direct affect upon the logic used for nesting. The independence of this option from the nesting allows us to arbitrarily chose domains where $\mu_h = 1$ and $\mu_h = 0$.

REFERENCES

1. T. L. Clark and R. D. Farley, *J. Atmos. Sci.* **41**, 329 (1984).
2. T. L. Clark, *J. Comput. Phys.* **24**, 186 (1977).
3. T. L. Clark, *J. Atmos. Sci.* **36**, 2191 (1979).
4. M. Vinokur, *J. Comput. Sci.* **14**, 105 (1974).
5. H. J. Stetter, *Numer. Math.* **29**, 425 (1978).
6. M. Ogura, *J. Meteorol. Soc. Japan* **47**, 319 (1969).
7. Y. Ogura and N. A. Phillips, *J. Atmos. Sci.*, **19**, 173 (1962).
8. E. Kessler, "On the Distribution and Continuity of Water Substance in Atmospheric Circulations," in *Meteor. Monogr. No.32* (Amer. Meteor. Soc., Boston, 1969), p. 84.
9. L. R. Koenig and F. W. Murray, *J. Appl. Meteorol.* **15**, 747 (1976).

[redacted]

12. G. P. Klaassen and T. L. Clark, *J. Atmos. Sci.* **42**, 2621 (1985).
13. P. K. Smolarkiewicz, *Mon. Weather Rev.* **111**, 479 (1983).
14. P. K. Smolarkiewicz, *J. Comput. Phys.* **54**, 325 (1984).
15. P. K. Smolarkiewicz and T. L. Clark, *J. Comput. Phys.*, **67**, 396 (1986).
16. A. Arakawa, *J. Comput. Phys.* **1**, 119 (1966).
17. D. K. Lilly, *Mon. Weather Rev.* **93**, 11 (1965).
18. T. Gal-Chen and R. C. J. Somerville, *J. Comput. Sci.* **17**, 209 (1975).
19. G. A. Dalu, *Q. J. Roy. Meteorol. Soc.* **104**, 797 (1978).
20. B. R. Ross and I. Orlanski, *J. Atmos. Sci.* **39**, 296 (1982).
21. J. A. Young and C. W. Hirt, *J. Fluid Mech.* **56**, 265 (1972).
22. I. Orlanski, *J. Comput. Phys.* **21**, 251 (1976).
23. N. A. Phillips and J. Shukla, *J. Appl. Meterol.* **12**, 763 (1973).
24. F. G. Schuman, in *Proceedings of the International Symposium on Numerical Weather Prediction, Tokyo, Japan, 1962* (Meteorol. Soc. Japan, 1962), p. 85.
25. L. N. Trefethen, *Siam Rev.* **24**, 113 (1982).